Check for updates

Relativistic electronic structure and photovoltaic performance of K₂CsSb†

Ruiqi Wu [ID] and Alex M. Ganose [ID]*

The discovery of an efficient and cost-effective photovoltaic absorber is urgently needed to meet global emission targets. Antimony-based materials have emerged as promising non-toxic and earth-abundant candidates with similar electronic properties to the lead hybrid perovskites. The full-Heusler K_2CsSb has been widely studied as a photocathode and thermoelectric material but has not been evaluated as a potential photovoltaic absorber. Here, using relativistic hybrid density functional theory, we demonstrate that K_2CsSb exhibits ideal properties for use in photovoltaic applications, based on its bandgap, dispersive conduction band, and strong optical absorption. Using a detailed balance approach, we reveal the maximum theoretical efficiency to be competitive with other state-of-the-art photovoltaics, reaching over 28 percent at a thickness of 200 nm. Additionally, we perform band-alignment calculations to provide recommendations for suitable device architectures that will minimise contact losses.

Introduction

With increasing global energy consumption, electricity generation from renewable sources including hydropower, solar, and wind is the main strategy for controlling annual temperature growth and related environmental problems. In 2021, the percentage of electricity generated from renewables saw an annual growth of 7%, with the majority originating from

Department of Chemistry, Molecular Sciences Research Hub, White City Campus, Imperial College London, Wood Lane, London, UK. E-mail: a.ganose@imperial.ac.uk
† Electronic supplementary information (ESI) available. See DOI: https://doi.org/10.1039/d3ta02061d

Dr Alex Ganose is a Lecturer and EPSRC Fellow in the Department of Chemistry at Imperial College London. Alex received his EngD from University College London in 2018 working with Professor David Scanlon, before moving to a postdoctoral position at Lawrence Berkeley National Laboratory with Dr Anubhav Jain. In 2021, he joined Imperial as an EPSRC Fellow and in 2022 he was appointed as a Lecturer. His research uses computational materials chemistry, machine learning, and data science to design new materials for renewable energy generation and energy storage.

photovoltaics together with wind power.[1] In comparison to solar energy captured chemically through oxidation and reduction reactions, solar photovoltaics show improved performance with maximum power conversion efficiencies of around 33% and 42% for single and multijunction devices, respectively. At present, silicon-based photovoltaics play an important role in the world's photovoltaics markets, accounting for approximately 95% of solar power generated in 2021.[2] However, manufacturing silicon wafers is energy intensive and requires thick films due to the indirect bandgap of silicon. The discovery of a cost-effective photovoltaic material with earth-abundant elements, high efficiency, and high stability under ambient conditions is urgently needed if the world is to reach renewable energy targets.

Since being discovered in 1903,[3] compounds with the full Heusler structure X_2YZ (where X and Y are transition metals, and Z is a main group element) have been studied for a wide range of applications, including spintronics, superconductors, multiferroics, and topological insulators. Compared to conventional full Heuslers with 24 valence electrons, the class of 8 valence electron Heuslers containing alkali metals exhibit low thermal conductivity and favourable electronic transport properties.[4–6] Among this class of materials, the ternary K_2CsSb has been extensively studied as a high-sensitivity photocathode for particle accelerators and scintillators, with state-of-the-art quantum efficiencies reaching over 10% and broad-band optical absorption covering the entire visible spectrum.[7–9] More recently, K_2CsSb was identified as a potential thermoelectric material in a high-throughput screening study of binary semiconductors.[10] Subsequent theoretical calculations revealed that K_2CsSb possesses an ultra-low lattice thermal conductivity

of 0.2 W m^{-1} K^{-1} and a predicted p-type ZT over 5 at 800 K, one of the largest ZTs of any material to date.[11]

Although K$_2$CsSb has received much attention as a photocathode and thermoelectric material, it has not been investigated as a potential photovoltaic absorber. This is despite its appealing composition of non-toxic elements, large predicted carrier mobility greater than 450 cm^2 V^{-1} s^{-1} at room temperature, broad-band optical absorption,[12] and a relatively low temperature (~90 °C sputtering) synthesis route.[13] The band gap of K$_2$CsSb, determined to be 1.2 eV from photoconductivity measurements[14] and ~1.6 eV from GW calculations,[9] falls within the ideal range for a photovoltaic absorber (namely 1.1–1.6 eV following the detailed balance limit). Furthermore, the ultralow thermal conductivity, like that seen in K$_2$CsSb, has been associated with a hot-phonon bottleneck mechanism that facilitates the extraction of higher energy carriers in CH$_3$NH$_3$PbI$_3$.[15]

Antimony-based materials have recently attracted considerable attention as photovoltaic absorbers. This is, in part, due to the success of the hybrid halide perovskites and the similarities in the electronic structures of antimony and lead.[16] Antimony selenide (Sb$_2$Se$_3$) is one such material that has seen remarkable progress in the last decade, with power conversion efficiencies reaching over 10% in 2022.[17] However, the current generation of antimony-based absorbers are typically low-dimensional semiconductors with quasi-1D connectivity. This arises from antimony's 5s^{2}5p^0 electronic configuration due to the formation of a stereochemically active lone pair.[18] Accordingly, these materials typically display larger effective masses (~0.4–1.0m_0) than other state-of-the-art photovoltaics and exhibit complex defect energy landscapes, with unusual four-electron negative-U vacancies observed in Sb$_2$Se$_3$.[19] In contrast, K$_2$CsSb crystallises in a highly symmetric face-centred cubic structure and will therefore exhibit isotropic absorption and transport behaviour. Here, antimony adopts an Sb^{3-} oxidation state with a full 5s^{2}5p^6 outer shell configuration that avoids the issues of stereochemical activity whilst still providing beneficial relativistic effects that increase the dispersion of the unoccupied 6s states forming the conduction band. Accordingly, K$_2$CsSb warrants further exploration as a potential photovoltaic candidate.

In this work, we assess the potential of K$_2$CsSb as a photovoltaic absorber using relativistic hybrid density functional theory. We reveal it possesses an ideal band gap of 1.6 eV, small conduction band effective mass of ~0.17m_0, and intense visible light absorption due to a secondary band pocket just above the fundamental band edge. Detailed balance calculations indicate K$_2$CsSb is competitive with state-of-the-art absorbers, with maximum theoretical efficiency greater than 28% for 200 nm thin films. By performing band alignment analysis we provide guidance on the choice of contact materials for an optimal device architecture. We highlight that attention should be paid to the choice of electron contact layer due to the small electron affinity when compared to existing photovoltaic technologies. Our work suggests that K$_2$CsSb shows promise as a novel earth-abundant photovoltaic candidate.

Methodology

We employ Kohn–Sham density-functional theory (DFT)[20] for all calculations in this work. Calculations were performed using the Vienna *Ab initio* Simulation Package (VASP),[21–24] with interactions between core and valence electrons described using the projector augmented wave (PAW) method.[25] The plane wave energy cutoff and k-point mesh were converged to a tolerance of 5 eV per atom and 1 eV per atom respectively. Ground state calculations used a plane-wave energy cutoff of 300 eV and a 6 × 6 × 6 Γ-centred k-point mesh. For optical absorption calculations, a 10 × 10 × 10 Γ-centred k-point mesh was needed to provide convergence. Geometry optimisation was performed using the PBEsol functional,[26] a version of the PBE functional[27] revised for solids. The convergence criteria for energy and forces were set to 10^{-8} eV and 10 meV Å^{-1}. To provide a more accurate description of optoelectronic properties, band structures, density of states, and optical absorption calculations were performed using the Heyd–Scuseria–Ernzerhof hybrid functional (HSE06)[28,29] which is known to provide band gap estimates in agreement with experiments for a wide range of materials.[30,31] The inclusion of spin–orbit coupling (SOC) effects was essential to describe optoelectronic properties accurately due to the presence of the heavy atom Sb. This combination of HSE + SOC has been shown to provide a reliable description of the electronic properties for a range of antimony[32,33] and bismuth[34] containing materials. The SUMO[35] package was used to calculate band edge effective masses and visualise band structure and optical absorption diagrams.

Crystal orbital Hamilton population (COHP) calculations were performed using the LOBSTER package to visualize bonding types between atomic orbitals.[36] The ionic contribution to the static dielectric constant was obtained from density functional perturbation theory (DFPT) calculations performed using the PBEsol functional.[37] The high-frequency dielectric response was calculated using HSE + SOC through the frequency-dependent microscopic polarisability matrix as implemented in VASP.[37] We note that higher-level methods such as time-dependent DFT have been applied to study the optical response of Heusler and related compounds;[38] however, due to computational restrictions we have not used this method in our work. To analyse the upper radiative limit of thickness-dependent energy conversion, we applied the "Spectroscopic Limited Maximum Efficiency" (SLME)[39] approach and the detailed balance method proposed by Blank *et al.*[40] Band alignment calculations were performed using a slab model constructed *via* the SURFAXE package[41] with a slab and vacuum thickness of 30 Å each. The (110) surface was used due to the lack of a surface dipole and low surface energy.

Vibrational properties were calculated within the harmonic approximation using the finite displacement method as implemented in the PHONOPY package.[42] A 3 × 3 × 3 supercell of the conventional lattice was found to provide convergence of the phonon eigenvalues. Phonon calculations were performed using the PBEsol functional, with the structure relaxed to a tighter force convergence criterion of 0.1 meV Å^{-1}. Finite

This journal is © The Royal Society of Chemistry 2023

J. Mater. Chem. A, 2023, **11**, 21636–21644 | **21637**

displacements were performed with a 700 eV energy cutoff and Γ-centered $2 \times 2 \times 2$ k-point mesh.

Results and discussion

Crystal structure

The geometry of K_2CsSb (space group $Fm\bar{3}m$) follows the typical X_2YZ full Heusler structure where the 8c $(\frac{1}{2}, \frac{1}{2}, \frac{1}{2})$ Wyckoff positions are occupied by the most electronegative element X (K), the less electronegative alkali metal Y (Cs) atoms occupy the 4b $(\frac{1}{2}, \frac{1}{2}, \frac{1}{2})$ sites, and the main group element Z (Sb) occupies the 4a $(0,0,0)$ sites.[43] In K_2CsSb, the K sites form a simple cubic sublattice, while Cs and Sb form an interpenetrated rocksalt sublattice (Fig. 1). The formal oxidation states are K^{1+}, Cs^{1+}, and Sb^{3-}, with each species displaying a fully occupied outer shell of electrons. This is responsible for the semiconducting behaviour observed in Heusler alloys. The K_2CsSb structure was fully optimised using the PBEsol functional. We find excellent agreement with the experimental lattice parameter, with the cell lengths reproduced to within 0.67%. This small degree of lattice shrinkage can be explained by the lack of temperature effects in our calculations. Our work is consistent with other theoretical calculations on K_2CsSb as highlighted in Table S1 of the ESI.†

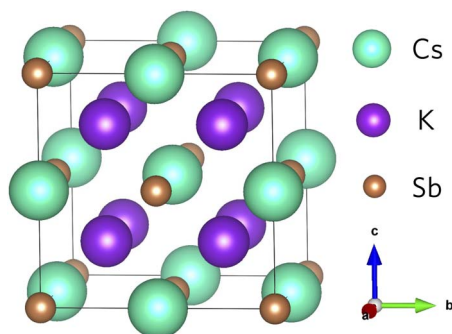**Fig. 1** Crystal structure of K_2CsSb. Teal, purple, and brown spheres represent Cs, K and Sb atoms, respectively.

To assess the dynamical stability of K_2CsSb, we further calculate vibrational properties within the harmonic approximation. The phonon dispersion diagram presented in Fig. S2 of the ESI† reveals the absence of imaginary modes, highlighting the stability of the ground state structure. To investigate the thermodynamic stability of K_2CsSb, we employed convex hull analysis to calculate the energy above hull against all competing elemental, secondary, and ternary phases in the Materials Project database. We find the energy above hull above to be zero, indicating that the material is stable with respect to decomposition. Accordingly, our calculations highlight the thermodynamic and dynamical stability of K_2CsSb as is also observed in experiments.

Electronic properties

The projected density of states calculated using HSE + SOC is presented in Fig. 2a. The valence band maximum is dominated by Sb 5p states, whereas the conduction band minimum is a mixture of Sb 6s, Cs d, and K d contributions. The orbital projection scheme fails to capture a significant portion of the total density of states in the conduction band. As we shall demonstrate, this is a consequence of a highly delocalised electron density that fills the interatomic voids in the crystal structure and gives rise to very small electron effective masses.

The Sb 5p states at the valence band edge are largely non-bonding in character. This is confirmed through the COHP analysis presented in Fig. 2b, which provides an indication of the type (bonding *vs.* antibonding) and strength of orbital interactions. Despite a strongly localised peak in the density of states, the COHP analysis reveals a much smaller negative peak at the valence band edge indicating weakly antibonding/nonbonding interactions. This can be rationalised by considering the partial charge density isosurfaces of the valence band maximum presented in Fig. 3a. The isosurface indicates a spherical electron density surrounding the antimony sites (corresponding to the fully filled Sb 5p orbitals), with no other orbital interactions present. The fully filled Sb 5s, K 3p and Cs 5p orbitals are found much deeper inside the valence band and
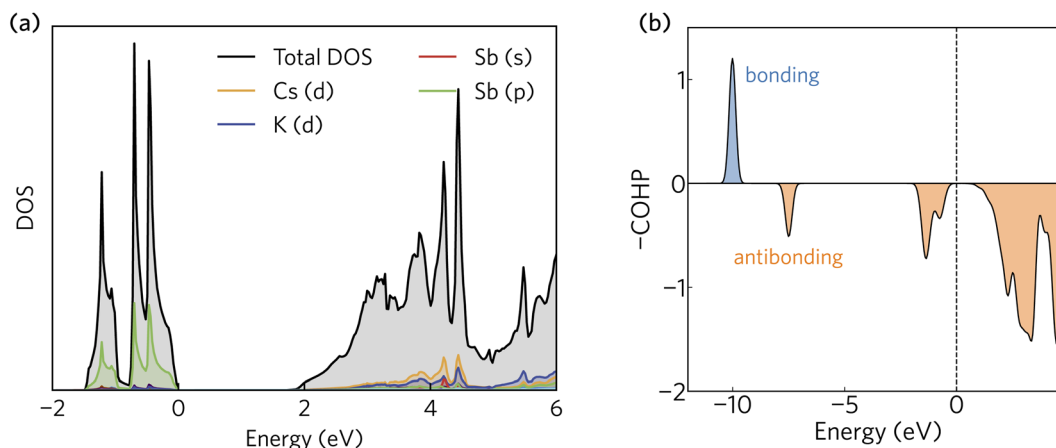

Fig. 2 (a) The density of states and (b) crystal orbital Hamilton population (COHP) analysis of K_2CsSb calculated using HSE + SOC. In (a) and (b), the valence band maximum has been set to zero eV.

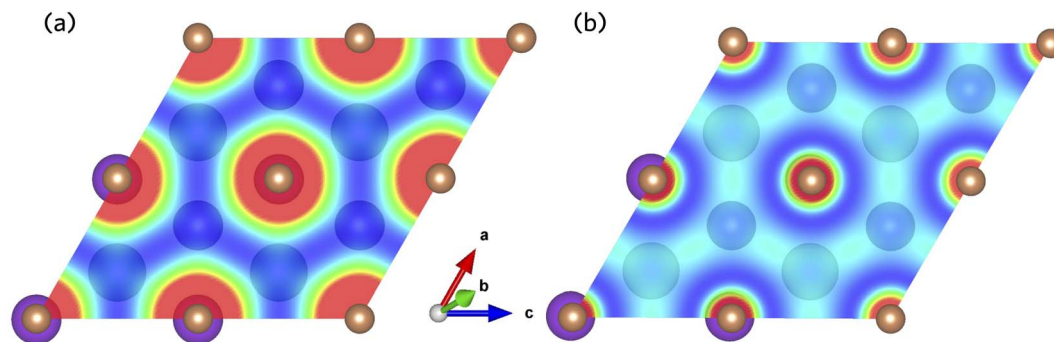**21638** | *J. Mater. Chem. A*, 2023, **11**, 21636–21644

This journal is © The Royal Society of Chemistry 2023

Fig. 3 Partial charge density isosurfaces for the (a) valence band maximum and (b) conduction band minimum of K_2CsSb calculated using HSE + SOC.

can be considered semicore states (see Fig. S2 in the ESI†). In contrast, the conduction band minimum exhibits strongly antibonding character, as indicated by the large negative peak above the Fermi level in the COHP analysis (Fig. 2b). As can be observed in the partial charge density isosurface of the conduction band minimum, the Sb 6s states are mixed with higher energy unoccupied alkali orbitals to form channels throughout the crystal, resulting in a "sponge" like structure. The obvious lack of charge density between the antimony s states and the almost free electron density between the atoms highlights the antibonding character of these states.

The electronic band structure of K_2CsSb, calculated using HSE + SOC, is presented in Fig. 4. The band structure displays a direct band gap of 1.59 eV at the Γ-point, within the ideal range for a photovoltaic absorber between 1.1 and 1.6 eV. We find relatively strong relativistic renormalisation of the band gap (0.183 eV) due to the presence of heavy antimony atoms. The renormalisation mainly originates from the valence band maximum, which is raised by 0.179 eV due to spin splitting. This is considerably larger than seen in other antimony-based absorbers such as Sb_2Se_3 which exhibits relativistic renormalisation on the order of 0.05 eV.[44] We note the calculated band gap is significantly overestimated compared to experiment.
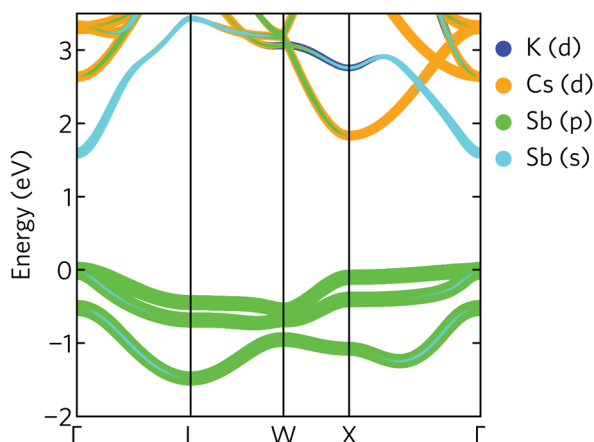
Photoconductivity measurements on K_2CsSb thin films suggest a band gap of 1.2 eV.[14] The origin of this discrepancy is unclear. One possible explanation is the absence of lattice expansion and electron–phonon coupling in our calculations that can act to renormalise the gap. Regardless, our results are in agreement with a recent GW study that reported a band gap of 1.62 eV.[9]

The valence band maximum is relatively dispersionless with strong antimony p character (Fig. 4), in agreement with the calculated density of states and partial charge density isosurfaces. In contrast, the conduction band minimum is highly dispersive and largely composed of antimony s character. We also note a secondary conduction band pocket at the X high-symmetry point, with a direct gap of 1.85 eV, only slightly larger than the fundamental gap at Γ. This secondary minimum has mainly Cs d character, with some Sb p mixing away from the band edge.

To better understand the carrier transport properties of K_2CsSb, we calculated band edge effective masses using the SUMO package.[35] The effective masses of the valence band maximum and conduction band minimum are listed in Table 1. The conduction band minimum exhibits very small electron effective masses of $0.17m_0$ in both the $\Gamma \rightarrow L$ and $\Gamma \rightarrow X$ high-symmetry directions. This is comparable to state-of-the-art photovoltaics such as $CH_3NH_3PbI_3$ ($m_e = 0.15m_0$)[45] and CdTe ($0.11m_0$) and considerably smaller than other Sb-containing absorbers including $CuSbSe_2$ ($0.71m_0$),[46] SbSI ($0.65m_0$),[47] and Sb_2Se_3 ($\sim0.35m_0$),[32] as well as other half-Heuslers such as RuNbSb ($0.71m_0$) and FeNbSb ($1.43m_0$)[48] and full-Heusler Fe_2VAl ($0.60m_0$).[49] The small electron effective masses in K_2CsSb originate from the high conduction bandwidth and "sponge" like delocalised nearly free electron density. Small effective masses are beneficial for charge extraction since photoexcited carriers have a greater chance of reaching the contact layers before recombining and generally result in large polarons, weakly bound excitons,[50] and small defect capture cross sections.[51] The hole effective masses in K_2CsSb are noticeably larger, with values of $1.01m_0$ (along $\Gamma \rightarrow L$) and $0.82m_0$ ($\Gamma \rightarrow X$). This is similar to other emerging bismuth- and antimony-based absorbers such as BiSI ($m_h = 0.95m_0$),[52] SbI_3 ($1.15m_0$),[53] and Sb_2Se_3 ($0.90m_0$),[32] which also display preferential electron transport behaviour.

Fig. 4 Projected band structure of K_2CsSb calculated using HSE + SOC. The valence band maximum is set to zero eV.

Table 1 Optoelectronic properties of K_2CsSb. The bandgap (E_g), effective masses of holes (m_h) and electrons (m_e), and high-frequency dielectric constant (ε_∞) were calculated using HSE + SOC. The static dielectric constant (ε_s) includes ionic contributions obtained using DFPT with the PBEsol functional. The Wannier–Mott exciton binding energy (E_b) was calculated using effective mass theory

| Compound	E_g (eV)	ε_∞	ε_s	E_b (meV)	m_e (m_0)		m_h (m_0)	
					$\Gamma \to L$	$\Gamma \to X$	$\Gamma \to L$	$\Gamma \to X$
K_2CsSb	1.589	6.11	14.02	9.9	0.17	0.17	1.01	0.82

Optical properties

A large dielectric constant is thought to play a key role in achieving defect tolerance by minimising trap-introduced non-radiative losses within photovoltaic devices.[16,54] This is due to the role the dielectric constant plays in the defect capture cross-sections. A large dielectric constant also screens charged impurities preventing defect scattering.[55] The high-frequency (ε_∞) and static (ε_s) dielectric constants of K_2CsSb were calculated to be 7.91 and 14.0, respectively. The relatively large difference between the two constants indicates that ionic screening due to longitudinal polar optical phonons plays a major role in the dielectric response. Due to the cubic symmetry the dielectric constants are isotropic. The calculated static dielectric constant is considerably smaller than those found in other ns^2 containing solar absorbers such as Sb_2Se ($\sim$75)[32] and $CH_3NH_3PbI_3$ (80),[56] which exhibit very large ionic screening due to the polarisability of the lone pair. However, it is comparable to well-established photovoltaics including silicon (11.7),[57] GaAs (12.90),[58] and CdTe (10.31).[59] We therefore expect a reasonable degree of charge screening will be observed in K_2CsSb.

The static dielectric constant can be used to calculate the Wannier–Mott exciton radius within effective mass theory as $a_0 = \varepsilon_s/\mu$ (in au), where the reduced effective mass $\mu = (m_e m_h)/(m_e + m_h)$. This gives an exciton radius of 52 Å and associated exciton binding energy ($E_b = 1/(2\varepsilon_s a_0)$) of 10 meV. This suggests that excitons will not play a significant role in photovoltaic device physics and are unlikely to be the origin of the discrepancy between the calculated and experimentally measured band gap.

In addition to the appropriate band gap and mobile charge carriers, strong visible light absorption is essential to achieve high photovoltaic efficiency. The optical absorption of K_2CsSb, calculated using HSE + SOC, is displayed in Fig. 5a. The absorption displays a steep onset, quickly reaching greater than 10^5 cm^{-1} within 0.7 eV of the fundamental bandgap. The sharp onset is competitive with other thin-film absorbers such as CdTe and the hybrid perovskites, and significantly stronger than indirect band gap absorbers such as silicon.[60] The strong absorption can be rationalised by the relatively flat valence band which increases the joint density of states near the fundamental gap. Furthermore, as detailed above, the secondary conduction band pocket at X will result in additional absorption at photon energies above 1.85 eV.

To evaluate the potential for K_2CsSb in photovoltaic applications, we calculated the thickness-dependent conversion efficiency using the "spectroscopic limited maximum efficiency" (SLME) model[39] and the detailed balance metric proposed by Blank et al.[40] The Blank approach extends the SLME metric by distinguishing the external luminescence yield from internal radiative recombination, with more details of this approach given in Section S7 of the ESI.† Both approaches used the frequency-dependent dielectric response calculated using HSE + SOC. The theoretical efficiency is strongly dependent on the thickness of the absorber layer, with the maximum
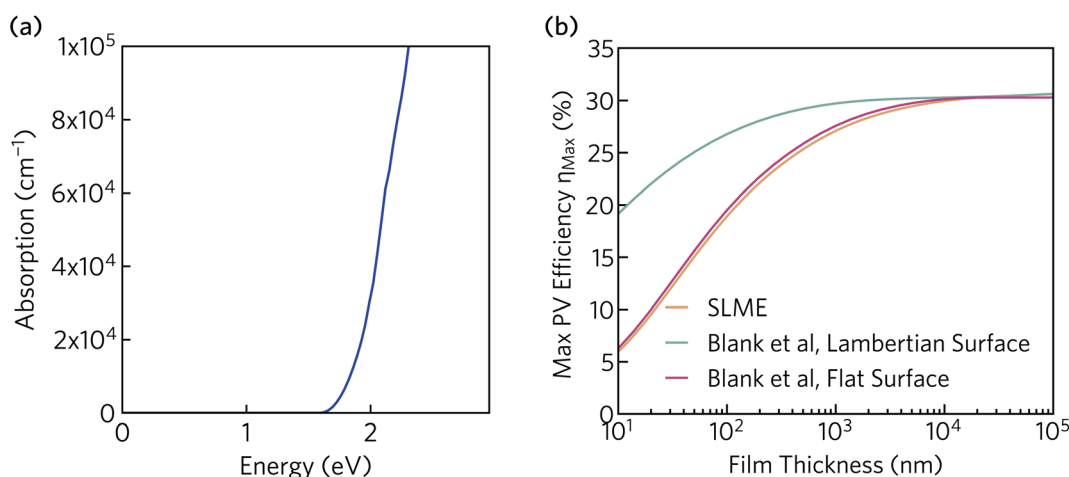
Fig. 5 (a) Optical absorption spectrum of K_2CsSb calculated using HSE + SOC. (b) Thickness-dependent theoretical maximum efficiency of K_2CsSb calculated using the "spectroscopic limited maximum efficiency" (SLME) method and detailed balance metric proposed by Blank et al.[40]

21640 | J. Mater. Chem. A, 2023, 11, 21636–21644

This journal is © The Royal Society of Chemistry 2023

efficiency reaching a plateau of 30% at a thickness of 10 μm. The Lambertian model reduces losses by simulating unity reflectance for the back surface and a diffusely scattering front surface, and exhibits higher efficiencies than both SLME and a flat surface for the same film thickness. At a thickness of 200 nm (appropriate for thin-film photovoltaics), the maximum efficiency is found to be over 28%. This is considerably larger than those predicted for Sb_2Se_3 and $NaSbS_2$ at the same film thickness (~10% (ref. 32) and 22.3%,[61] respectively) and comparable to those of other emerging absorbers such as $Sn_2SbS_2I_3$ (~29%).[33] We stress that these metrics provide an upper limit to the theoretical efficiency and do not take into account voltage losses due to non-radiative recombination and resistive interfaces. Regardless, these results highlight the potential for K_2CsSb as an absorber layer in photovoltaic devices.

Band alignment

To provide recommendations on the ideal device architecture of K_2CsSb devices, we performed band alignment calculations using a slab–vacuum model. An efficient band alignment between electron and hole contact layers can minimise barriers for carrier diffusion at interfaces and prevent open-circuit voltage losses. We note our calculations provide estimates of the "bulk" band alignment, and do not take into account relaxations and band bending at the surface. We calculate an ionisation potential and electron affinity of 1.82 eV and 3.42 eV, respectively. Our results differ somewhat from early experimental reports on K_2CsSb that observed an electron affinity of 1.1 eV through photoconductivity measurements.[62] The origin of this discrepancy is unclear, but could result from the relatively thin films used or reconstruction at the surface. Furthermore, our calculated results are for the bulk electronic structure, whereas experimental measurements will depend on the surface termination of the crystal. Regardless, these relatively small values mean that photons with energies greater than the ionisation potential could cause the emission of electrons through the photoelectric effect, preventing carrier

collection at the device contacts. To simulate the impact on the internal quantum efficiency due to photoemitted carriers, we perform the SLME metric with the absorption greater than the ionisation potential set to zero. We find very little change in the predicted theoretical efficiencies (less than 1%, see Fig. S5 in the ESI†). This can be rationalised since high-energy ultraviolet photons contribute a vanishing portion of the AM 1.5 solar spectrum. Accordingly, the impact of the small ionisation potential of photovoltaic performance is expected to be limited.

In Fig. 6, we compare the band alignment of K_2CsSb to a range of conventional and emerging photovoltaic absorbers. We find the electron affinity and ionisation potential of K_2CsSb to be much smaller than those of any other commonly used absorber.[67,68] For example, the ionisation potential of K_2CsSb is smaller than the *electron affinity* of both Si and AgCuS. The origin of the small ionisation potentials can be explained by the electronic configuration of antimony. In K_2CsSb, the 5p orbitals are fully occupied and form the valence band maximum, whereas in other common absorbers, the valence p states are either fully unoccupied (thereby forming the conduction band) or covalently bonded to give occupied bonding states and unoccupied antibonding states (the latter of which forms the conduction band).

The low ionisation potential and electron affinity of K_2CsSb will require judicious choice of contact materials to maximise the obtainable open-circuit voltage. For favourable electron transport throughout a device, the work function (Φ) of the transparent electron contact should be greater than the electron affinity of the absorber. Conversely, the work function of the hole contact layer should be smaller than the absorber's ionisation potential. Commonly used n-type transparent conductors have significantly deeper work functions (greater than 4 eV) and will not be appropriate for use with K_2CsSb. Accordingly, use of an ultralow work function n-type contact, such as the semiconducting polymer $TPHP(LiClO_4)$ ($\Phi = 2.2$ eV), will be necessary.[69] For the hole transport layer, a small work function metal alloy such as MgNd ($\Phi = 3.5$ eV) may be appropriate,[70]

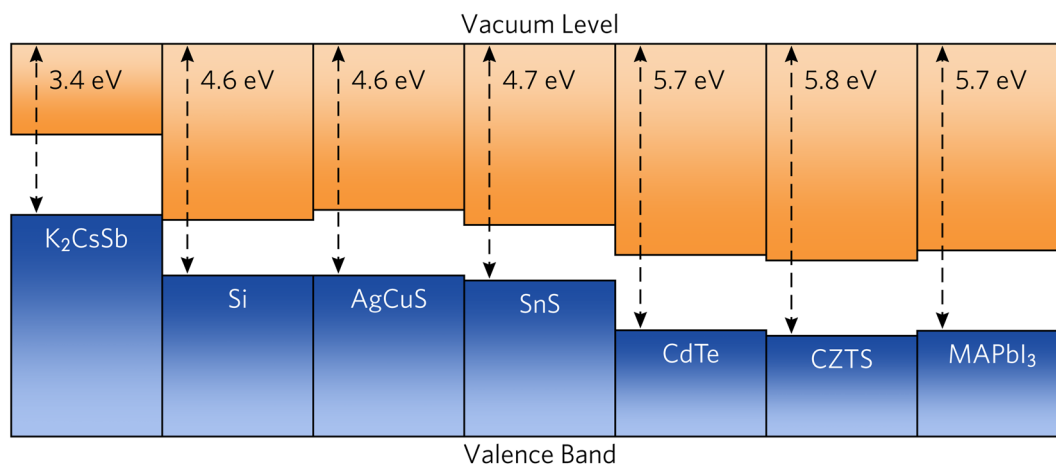**Fig. 6** Calculated band alignment of K_2CsSb compared to conventional and emerging photovoltaic absorbers. Electron affinity and bandgap data were taken from ref. 63–66.

This journal is © The Royal Society of Chemistry 2023

J. Mater. Chem. A, 2023, **11**, 21636–21644 | **21641**

although other contacts without expensive Nd would be preferred.

Conclusion

We have proposed K_2CsSb as a potential photovoltaic candidate based on relativistic density functional theory calculations. K_2CsSb possesses an ideal band gap of 1.59 eV, very small electron effective mass ($0.17m_0$), small predicted exciton binding energies, and strong optical absorption across the entire visible spectrum. We have highlighted the origin of the favourable electronic properties is a highly delocalised "sponge"-like electron density in the conduction band. The predicted maximum theoretical efficiency of 28% for a 200 nm thin film is competitive with other state-of-the-art absorbers. Furthermore, we performed band alignment calculations to provide suggestions for an optimised device architecture that can maximise open-circuit voltages. We believe K_2CsSb is a promising candidate photovoltaic absorber worthy of further study.

Author contributions

Ruiqi Wu: investigation, formal analysis, methodology, visualization, writing – original draft, writing – review & editing. Alex Ganose: conceptualization, methodology, resources, supervision, writing – review & editing.

Conflicts of interest

There are no conflicts to declare.

Acknowledgements

References

1 IEA, *Renewable Electricity – Analysis*, https://www.iea.org/reports/renewable-electricity, 2021.

2 D. S. Philipps, F. Ise, W. Warmuth and P. P. GmbH, *Photovoltaics Report*, 2022.

3 Deutsche Physikalische Gesellschaft (1899-1945), *Verhandlungen der Deutschen physikalischen Gesellschaft*; Friedr. Vieweg & Sohn, 1903.

4 P. D. Patel, S. B. Pillai, S. M. Shinde, S. D. Gupta and P. K. Jha, Electronic, Magnetic, Thermoelectric and Lattice Dynamical Properties of Full Heusler Alloy Mn₂RhSi: DFT Study, *Phys. B*, 2018, **550**, 376–382.

5 F. Gucci, T. G. Saunders, B. Srinivasan, F. Cheviré, D. A. Ferluccio, J.-W. G. Bos and M. J. Reece, Hybrid Flash-SPS of TiNiCu₀.₀₅Sn with Reduced Thermal Conductivity, *J. Alloys Compd.*, 2020, **837**, 155058.

6 C. S. Lue, C. F. Chen, J. Y. Lin, Y. T. Yu and Y. K. Kuo, Thermoelectric Properties of Quaternary Heusler Alloys Fe₂VAl₁₋ₓSiₓ, *Phys. Rev. B: Condens. Matter Mater. Phys.*, 2007, **75**, 064204.

7 L. Guo, M. Kuriki, A. Yokota, M. Urano and K. Negishi, Substrate Dependence of CsK₂Sb Photo-Cathode Performance, *Prog. Theor. Phys.*, 2017, **2017**, 033G01.

8 M. A. Mamun, C. Hernandez-Garcia, M. Poelker and A. A. Elmustafa, Correlation of CsK₂Sb Photocathode Lifetime with Antimony Thickness, *APL Mater.*, 2015, **3**, 066103.

9 C. Cocchi, S. Mistry, M. Schmeißer, J. Kühn and T. Kamps, First-Principles Many-Body Study of the Electronic and Optical Properties of CsK₂Sb, a Semiconducting Material for Ultra-Bright Electron Sources, *J. Phys.: Condens. Matter*, 2018, **31**, 014002.

10 G. Xing, J. Sun, Y. Li, X. Fan, W. Zheng and D. J. Singh, Electronic Fitness Function for Screening Semiconductors as Thermoelectric Materials, *Phys. Rev. Mater.*, 2017, **1**, 065405.

11 K. Yuan, X. Zhang, Z. Chang, D. Tang and M. Hu, Antibonding Induced Anharmonicity Leading to Ultralow Lattice Thermal Conductivity and Extraordinary Thermoelectric Performance in CsK₂X (X = Sb, Bi), *J. Mater. Chem. C*, 2022, **10**, 15822–15832.

12 T. Yue, P. Sui, Y. Zhao, J. Ni, S. Meng and Z. Dai, Theoretical Prediction of Mechanics, Transport, and Thermoelectric Properties of Full Heusler Compounds Na₂KSb and X₂CsSb (X = K, Rb), *Phys. Rev. B*, 2022, **105**, 184304.

13 M. Gaowei, Z. Ding, S. Schubert, H. B. Bhandari, J. Sinsheimer, J. Kuehn, V. V. Nagarkar, M. S. J. Marshall, J. Walsh, E. M. Muller, K. Attenkofer, H. J. Frisch, H. Padmore and J. Smedley, Synthesis and X-Ray Characterization of Sputtered Bi-Alkali Antimonide Photocathodes, *APL Mater.*, 2017, **5**, 116104.

14 C. Ghosh and B. P. Varma, Preparation and Study of Properties of a Few Alkali Antimonide Photocathodes, *J. Appl. Phys.*, 1978, **49**, 4549.

15 J. M. Frost, L. D. Whalley and A. Walsh, Slow Cooling of Hot Polarons in Halide Perovskite Solar Cells, *ACS Energy Lett.*, 2017, **2**, 2647–2652.

16 A. M. Ganose, C. N. Savory and D. O. Scanlon, Beyond Methylammonium Lead Iodide: Prospects for the Emergent Field of ns^2 Containing Solar Absorbers, *Chem. Commun.*, 2016, **53**, 20–44.

17 Y. Zhao, S. Wang, C. Li, B. Che, X. Chen, H. Chen, R. Tang, X. Wang, G. Chen, T. Wang, J. Gong, T. Chen, X. Xiao and J. Li, Regulating Deposition Kinetics *via* a Novel Additive-Assisted Chemical Bath Deposition Technology Enables Fabrication of 10.57%-Efficiency Sb₂Se₃ Solar Cells, *Energy Environ. Sci.*, 2022, **15**, 5118–5128.

18 A. Walsh, D. J. Payne, R. G. Egdell and G. W. Watson, Stereochemistry of Post-Transition Metal Oxides: Revision

21642 | *J. Mater. Chem. A*, 2023, **11**, 21636–21644

This journal is © The Royal Society of Chemistry 2023

of the Classical Lone Pair Model, *Chem. Soc. Rev.*, 2011, **40**, 4455–4463.

19 X. Wang, S. R. Kavanagh, D. O. Scanlon and A. Walsh, Four-Electron Negative-U Vacancy Defects in Antimony Selenide, *arXiv*, 2023, preprint, arXiv:2302.04901, DOI: **10.48550/arXiv.2302.04901**.

20 W. Kohn and L. J. Sham, Self-Consistent Equations Including Exchange and Correlation Effects, *Phys. Rev.*, 1965, **140**, A1133–A1138.

21 G. Kresse and J. Hafner, Ab Initio Molecular Dynamics for Liquid Metals, *Phys. Rev. B: Condens. Matter Mater. Phys.*, 1993, **47**, 558–561.

22 G. Kresse and J. Furthmüller, Efficient Iterative Schemes for *Ab Initio* Total-Energy Calculations Using a Plane-Wave Basis Set, *Phys. Rev. B: Condens. Matter Mater. Phys.*, 1996, **54**, 11169–11186.

23 G. Kresse and J. Hafner, Ab Initio Molecular-Dynamics Simulation of the Liquid-Metal–Amorphous-Semiconductor Transition in Germanium, *Phys. Rev. B: Condens. Matter Mater. Phys.*, 1994, **49**, 14251–14269.

24 G. Kresse and J. Furthmüller, Efficiency of *Ab Initio* Total Energy Calculations for Metals and Semiconductors Using a Plane-Wave Basis Set, *Comput. Mater. Sci.*, 1996, **6**, 15–50.

25 G. Kresse and D. Joubert, From Ultrasoft Pseudopotentials to the Projector Augmented-Wave Method, *Phys. Rev. B: Condens. Matter Mater. Phys.*, 1999, **59**, 1758–1775.

26 J. P. Perdew, A. Ruzsinszky, G. I. Csonka, O. A. Vydrov, G. E. Scuseria, L. A. Constantin, X. Zhou and K. Burke, Restoring the Density-Gradient Expansion for Exchange in Solids and Surfaces, *Phys. Rev. Lett.*, 2008, **100**, 136406.

27 J. P. Perdew, K. Burke and M. Ernzerhof, Generalized Gradient Approximation Made Simple, *Phys. Rev. Lett.*, 1996, **77**, 3865–3868.

28 A. V. Krukau, O. A. Vydrov, A. F. Izmaylov and G. E. Scuseria, Influence of the Exchange Screening Parameter on the Performance of Screened Hybrid Functionals, *J. Chem. Phys.*, 2006, **125**, 224106.

29 J. Heyd, G. E. Scuseria and M. Ernzerhof, Hybrid Functionals Based on a Screened Coulomb Potential, *J. Chem. Phys.*, 2003, **118**, 8207–8215.

30 J.-H. Pöhls, S. Chanakian, J. Park, A. M. Ganose, A. Dunn, N. Friesen, A. Bhattacharya, B. Hogan, S. Bux, A. Jain, A. Mar and A. Zevalkink, Experimental validation of high thermoelectric performance in RECuZnP$_2$ predicted by high-throughput DFT calculations, *Mater. Horiz.*, 2021, **8**, 209–215.

31 W. Travis, C. E. Knapp, C. N. Savory, A. M. Ganose, P. Kafourou, X. Song, Z. Sharif, J. K. Cockcroft, D. O. Scanlon, H. Bronstein and R. G. Palgrave, Hybrid Organic–Inorganic Coordination Complexes as Tunable Optical Response Materials, *Inorg. Chem.*, 2016, **55**, 3393–3400.

32 X. Wang, Z. Li, S. R. Kavanagh, A. M. Ganose and A. Walsh, Lone Pair Driven Anisotropy in Antimony Chalcogenide Semiconductors, *Phys. Chem. Chem. Phys.*, 2022, **24**, 7195–7202.

33 S. R. Kavanagh, C. N. Savory, D. O. Scanlon and A. Walsh, Hidden Spontaneous Polarisation in the Chalcohalide Photovoltaic Absorber Sn$_2$SbS$_2$I$_3$, *Mater. Horiz.*, 2021, **8**, 2709–2716.

34 A. M. Ganose, S. Matsumoto, J. Buckeridge and D. O. Scanlon, Defect Engineering of Earth-Abundant Solar Absorbers BiSI and BiSeI, *Chem. Mater.*, 2018, **30**, 3827–3835.

35 M. G. Alex, J. J. Adam and O. S. David, Sumo: Command-line Tools for Plotting and Analysis of Periodic *Ab Initio* Calculations, *J. Open Source Softw.*, 2018, **3**, 717.

36 R. Dronskowski and P. E. Bloechl, Crystal Orbital Hamilton Populations (COHP): Energy-Resolved Visualization of Chemical Bonding in Solids Based on Density-Functional Calculations, *J. Phys. Chem.*, 1993, **97**, 8617–8624.

37 M. Gajdoš, K. Hummer, G. Kresse, J. Furthmüller and F. Bechstedt, Linear Optical Properties in the Projector-Augmented Wave Methodology, *Phys. Rev. B: Condens. Matter Mater. Phys.*, 2006, **73**, 045112.

38 C. Lian, Z. A. Ali, H. Kwon and B. M. Wong, Indirect but Efficient: Laser-Excited Electrons Can Drive Ultrafast Polarization Switching in Ferroelectric Materials, *J. Phys. Chem. Lett.*, 2019, **10**, 3402–3407.

39 L. Yu and A. Zunger, Identification of Potential Photovoltaic Absorbers Based on First-Principles Spectroscopic Screening of Materials, *Phys. Rev. Lett.*, 2012, **108**, 068701.

40 B. Blank, T. Kirchartz, S. Lany and U. Rau, Selection Metric for Photovoltaic Materials Screening Based on Detailed-Balance Analysis, *Phys. Rev. Appl.*, 2017, **8**, 024032.

41 K. Brlec, D. W. Davies and D. O. Scanlon, Surfaxe: Systematic Surface Calculations, *J. Open Source Softw.*, 2021, **6**, 3171.

42 A. Togo, First-Principles Phonon Calculations with Phonopy and Phono3py, *J. Phys. Soc. Jpn.*, 2023, **92**, 012001.

43 *Heusler Alloys: Properties, Growth, Applications*, ed. Felser, C. and Hirohata, A., Springer Series in Materials Science, Springer International Publishing, Cham, 2016, vol. 222.

44 C. N. Savory and D. O. Scanlon, The Complex Defect Chemistry of Antimony Selenide, *J. Mater. Chem. A*, 2019, **7**, 10739–10744.

45 J. M. Frost, K. T. Butler, F. Brivio, C. H. Hendon, M. van Schilfgaarde and A. Walsh, Atomistic Origins of High-Performance in Hybrid Halide Perovskite Solar Cells, *Nano Lett.*, 2014, **14**, 2584–2590.

46 A. W. Welch, L. L. Baranowski, H. Peng, H. Hempel, R. Eichberger, T. Unold, S. Lany, C. Wolden and A. Zakutayev, Trade-Offs in Thin Film Solar Cells with Layered Chalcostibite Photovoltaic Absorbers, *Adv. Energy Mater.*, 2017, **7**, 1601935.

47 Y. C. Choi, E. Hwang and D.-H. Kim, Controlled Growth of SbSI Thin Films from Amorphous Sb$_2$S$_3$ for Low-Temperature Solution Processed Chalcohalide Solar Cells, *APL Mater.*, 2018, **6**, 121108.

48 T. Fang, S. Zheng, T. Zhou, L. Yan and P. Zhang, Computational prediction of high thermoelectric performance in p-type half-Heusler compounds with low band effective mass, *Phys. Chem. Chem. Phys.*, 2017, **19**, 4411–4417.

This journal is © The Royal Society of Chemistry 2023

J. Mater. Chem. A, 2023, **11**, 21636–21644 | **21643**

49 B. Hinterleitner, F. Garmroudi, N. Reumann, T. Mori, E. Bauer and R. Podloucky, The electronic pseudo band gap states and electronic transport of the full-Heusler compound Fe_2VAl, *J. Mater. Chem. C*, 2021, **9**, 2073–2085.

50 A. Walsh and A. Zunger, Instilling Defect Tolerance in New Compounds, *Nat. Mater.*, 2017, **16**, 964–967.

51 Y. Huang, H. Yuan and H. Chen, High-Performance Thermoelectrics in Two-Dimensional Layered AB_2Te_4 (A = Sn, Pb; B = Sb, Bi) Ternary Compounds, *Phys. Chem. Chem. Phys.*, 2022, 1808–1818.

52 D. Tiwari, F. Cardoso-Delgado, D. Alibhai, M. Mombrú and D. J. Fermín, Photovoltaic Performance of Phase-Pure Orthorhombic BiSI Thin-Films, *ACS Appl. Energy Mater.*, 2019, **2**, 3878–3885.

53 P. Liu, F. Lu, M. Wu, X. Luo, Y. Cheng, X.-W. Wang, W. Wang, W.-H. Wang, H. Liu and K. Cho, Electronic Structures and Band Alignments of Monolayer Metal Trihalide Semiconductors MX_3, *J. Mater. Chem. C*, 2017, **5**, 9066–9071.

54 R. Su, Z. Xu, J. Wu, D. Luo, Q. Hu, W. Yang, X. Yang, R. Zhang, H. Yu, T. P. Russell, Q. Gong, W. Zhang and R. Zhu, Dielectric Screening in Perovskite Photovoltaics, *Nat. Commun.*, 2021, **12**, 2479.

55 A. M. Ganose, J. Park, A. Faghaninia, R. Woods-Robinson, K. A. Persson and A. Jain, Efficient Calculation of Carrier Scattering Rates from First Principles, *Nat. Commun.*, 2021, **12**, 2222.

56 S. Govinda, B. P. Kore, M. Bokdam, P. Mahale, A. Kumar, S. Pal, B. Bhattacharyya, J. Lahnsteiner, G. Kresse, C. Franchini, A. Pandey and D. D. Sarma, Behavior of Methylammonium Dipoles in $MAPbX_3$ (X = Br and I), *J. Phys. Chem. Lett.*, 2017, **8**, 4113–4121.

57 W. C. Dunlap and R. L. Watters, Direct Measurement of the Dielectric Constants of Silicon and Germanium, *Phys. Rev.*, 1953, **92**, 1396–1397.

58 W. J. Moore and R. T. Holm, Infrared Dielectric Constant of Gallium Arsenide, *J. Appl. Phys.*, 1996, **80**, 6939–6942.

59 I. Strzalkowski, S. Joshi and C. R. Crowell, Dielectric Constant and Its Temperature Dependence for GaAs, CdTe, and ZnSe, *Appl. Phys. Lett.*, 1976, **28**, 350–352.

60 S. De Wolf, J. Holovsky, S.-J. Moon, P. Löper, B. Niesen, M. Ledinsky, F.-J. Haug, J.-H. Yum and C. Ballif, Organometallic Halide Perovskites: Sharp Optical Absorption Edge and Its Relation to Photovoltaic Performance, *J. Phys. Chem. Lett.*, 2014, **5**, 1035–1039.

61 W. W. W. Leung, C. N. Savory, R. G. Palgrave and D. O. Scanlon, An Experimental and Theoretical Study into $NaSbS_2$ as an Emerging Solar Absorber, *J. Mater. Chem. C*, 2019, **7**, 2059–2067.

62 R. Nathan and C. H. B. Mee, Photoelectric and Related Properties of the Potassium—Antimony—Caesium Photocathode, *Int. J. Electron.*, 1967, **23**, 349–354.

63 L. A. Burton and A. Walsh, Band Alignment in SnS Thin-Film Solar Cells: Possible Origin of the Low Conversion Efficiency, *Appl. Phys. Lett.*, 2013, **102**, 132111.

64 J. Brgoch, A. J. Lehner, M. Chabinyc and R. Seshadri, *Ab Initio* Calculations of Band Gaps and Absolute Band Positions of Polymorphs of $RbPbI_3$ and $CsPbI_3$: Implications for Main-Group Halide Perovskite Photovoltaics, *J. Phys. Chem. C*, 2014, **118**, 27721–27727.

65 C. N. Savory, A. M. Ganose, W. Travis, R. S. Atri, R. G. Palgrave and D. O. Scanlon, An Assessment of Silver Copper Sulfides for Photovoltaic Applications: Theoretical and Experimental Insights, *J. Mater. Chem. A*, 2016, **4**, 12648–12657.

66 A. Walsh, Principles of Chemical Bonding and Band Gap Engineering in Hybrid Organic–Inorganic Halide Perovskites, *J. Phys. Chem. C*, 2015, **119**, 5755–5760.

67 T. J. Whittles, L. A. Burton, J. M. Skelton, A. Walsh, T. D. Veal and V. R. Dhanak, Band Alignments, Valence Bands, and Core Levels in the Tin Sulfides SnS, SnS_2, and Sn_2S_3: Experiment and Theory, *Chem. Mater.*, 2016, **28**, 3718–3726.

68 G. Teeter, X-Ray and Ultraviolet Photoelectron Spectroscopy Measurements of Cu-doped CdTe(111)-B: Observation of Temperature-Reversible Cu_xTe Precipitation and Effect on Ionization Potential, *J. Appl. Phys.*, 2007, **102**, 034504.

69 B. Tong, J. Du, L. Yin, D. Zhang, W. Zhang, Y. Liu, Y. Wei, C. Liu, Y. Liang, D.-M. Sun, L.-P. Ma, H.-M. Cheng and W. Ren, A Polymer Electrolyte Design Enables Ultralow-Work-Function Electrode for High-Performance Optoelectronics, *Nat. Commun.*, 2022, **13**, 4987.

70 K. Ge, J. Chen, B. Chen, Y. Shen, J. Guo, F. Li, H. Liu, Y. Xu and Y. Mai, Low Work Function Intermetallic Thin Film as a Back Surface Field Material for Hybrid Solar Cells, *Sol. Energy*, 2018, **162**, 397–402.

21644 | *J. Mater. Chem. A*, 2023, **11**, 21636–21644

This journal is © The Royal Society of Chemistry 2023